# Kossel interferences of proton-induced X-ray emission lines to study thin film waveguides

J.P. Zhang, C. Pendenque, K. Le Guen, R. Delaunay, I. Vickridge, D. Schmaus, Q.G. Fu, P. Jonnard

# Kossel interferences of proton-induced X-ray emission lines to study thin film waveguides

J.P. Zhang[1,2*], C. Pendenque[1], K. Le Guen[1], R. Delaunay[1], I. Vickridge[3], D. Schmaus[3], Q.G. Fu [2], P. Jonnard[1*]

[1] *Sorbonne Université, CNRS UMR 7614, Laboratoire de Chimie Physique - Matière et Rayonnement, 4 place Jussieu, F-75252 Paris cedex 05, France*

[2] *State Key Laboratory of Solidification Processing, Shaanxi Key Laboratory of Fiber Reinforced Light-Weight Composites, Northwestern Polytechnical University, Xi'an 710072, China*

[3] *Sorbonne Université, CNRS UMR 7588, Institut des NanoSciences de Paris, 4 place Jussieu, F-75252 Paris cedex 05, France*

[*] **Corresponding author**s

philippe.jonnard@courriel.upmc.fr

jiaping.zhang@etu.upmc.fr

## Abstract

Proton-induced X-ray emission (PIXE) combined in Kossel geometry was developed as a non-destructive structural characterization method of nanometer thin films deposited on Si. The method is applied to study Pt/Fe/Pt and Ta/Cr/Pt thin films designed as X-ray planar waveguides. With the help of an energy dispersive X-ray camera, the intensities of characteristic X-ray emissions versus the detection angle (grazing exit), called Kossel curves, were measured. It is found that an interfacial compound is formed in Pt/Fe/Pt waveguide, whereas oxidation and mixing occur in the Ta/Cr/Pt system. It was not possible to obtain the description of the successive layers when considering only grazing incidence x-ray reflectivity. When PIXE-Kossel experiments are also considered, supplementary constraints have to be fulfilled when fitting the values of the stack parameters (number, composition, thickness, roughness and density of the layers) which restrict the possible descriptions of waveguides. Thus PIXE-Kossel is suitable to characterize stacks of nanometer thin films designed to be applied as an x-ray waveguide.

Keywords: X-ray waveguide; thin film; PIXE; Kossel diffraction; X-ray reflectometry

## 1. Introduction

Kossel interferences, evidenced by Walther Kossel in 1935 [1], are the typical diffraction patterns of the characteristic X-rays emitted within a crystalline structure and sensitive to the structure itself. Since 1970s, it has been applied as a tool to investigate the crystallographic orientations and lattice parameters [2-4]. The observation of Kossel interferences requires two steps. Firstly, to produce the characteristic X-ray emissions, an ionization source is necessary to generate the electron transitions. Then the produced X-ray emissions are diffracted by the periodic structure itself.

The ionization source can be energetic electrons [5-7], X-ray photons [8, 9], charged particles including protons or ions [10, 11]. Kossel diffraction associated to X-rays is related to the grazing exit X-ray fluorescence (GEXRF) technique [2, 12]. GEXRF measurement representing the angular resolved X-ray fluorescence technique, is sensitive to the elemental depth distributions in the nanometer range [13, 14]. It can be used as a complementary characterization method of X-ray reflectometry (XRR). In XRR measurements, the spectra are acquired by varying the incident angle in the grazing incidence regime while detecting the specular reflected X-ray beam. This technique uses the average electron density of a layer and thus cannot provide information on the elemental composition. By the combination of XRR and XRF analysis, we could overcome the limitations of XRR when dealing with elemental distributions and lateral inhomogeneities of multilayers [15-19]. For example, P. Hönicke et al. characterized the ultra-shallow Al-implanted silicon wafers by the combination of XRR and GIXRF [19].

In our previous works [12, 20, 21], we develop a methodology, that is particle-induced X-ray emission (PIXE) combined with Kossel diffraction, to study the structure of nano-scale Cr/Sc and Pd/Y periodic multilayers. PIXE analysis possesses a good sensitivity to measure the radiations emitted by electron state changes and distinguishes the elements of the sample in a wide range of atomic numbers, without destruction of the sample [11, 22]. In Ref. [12, 20, 21], the

generated X-ray emission is recorded in Kossel geometry to obtain the so-called Kossel curve, which is the intensity of characteristic X-ray emission as a function of the detection angle. Kossel curves are convenient to study the interfacial environment in multilayers made of a periodic alternation of nanometer-thick films.

Compared with other ionization excitation sources, electron excitation for example, the main advantage of proton excitation is the enhanced sensitivity due to substantial reduction of the primary beam bremsstrahlung [23]. This makes it possible to obtain reliable Kossel curves from small amounts of material: either very thin layers or from elements present in low concentrations. A second advantage is that, within the thickness of typical structures investigated by PIXE-Kossel, proton trajectories within the structure are rectilinear/straight. The target atoms may be assumed to be uniformly ionized throughout the thickness of the films, which could possess well-known ionization cross sections and x-ray emission probabilities. The sensitivity of the Kossel curve to sample structure (depth resolution) depends only on the X-ray transport properties of the structure: there is no intrinsic influence of the excitation source here. However, according to the comparison of measured/simulated Kossel curves, the noisiness of the observed curve will influence the confidence with which different possible sample structures can be differentiated/discriminated. In this case, compared with electron excitation, the lower primary beam bremsstrahlung and the "cleaner" X-ray spectra obtained upon proton irradiation are also clear advantages. The above merits significantly contribute to simplify the analysis of Kossel curves. Let us note that X-rays can also be used as a source with an excitation depth that can be up to 1 mm. Such an excitation also produces a low bremsstrahlung radiation. Moreover, as in this case the technique is photon-in photon-out, it can be applied on insulating sample, for example on multilayers deposited on silica substrates.

Instead of multilayers, generally made of a few tens of layers, the aim of this study is to check the feasibility of this method when used in non-periodic stacks consisting in only a few layers. To observe well-contrasted Kossel curves, the stack is an x-ray planar waveguide formed of three layers. Waveguides are designed to locate and concentrate the electric field of the emitted radiation in a specific layer of the

stack, thus being sensitive to the depth distribution of the emitting atoms. Here, Pt/Fe/Pt and Ta/Cr/Pt samples are designed, deposited on Si and then investigated by the PIXE-Kossel method. By comparing the experimental and simulated Kossel curves in order to obtain the description of the actual stack, the possible application of the PIXE-Kossel method is discussed.

## 2. Experimental

### 2.1. Design and fabrication of the thin film waveguides

Planar X-ray waveguides can be used as a focusing tool to produce nanometer-sized X-ray beams [24-26]. The structure generally consists of a low-Z layer sandwiched between two high-Z layers [27]. In the waveguide, the X-rays propagate with total internal reflection at the interfaces between the high- and low-Z layers. So, it is promising to study the feasibility of PIXE-Kossel for the structural characterization of planar X-ray waveguides.

In this study, in the process for designing planar X-ray waveguide, we first performed electric field depth distribution simulations to optimize the structural parameters (including elements and thickness) using IMD software [28]. Interfacial and substrate roughness were assumed to be zero for the simulations. Two thin films waveguides were designed: Pt(4 nm)/Fe(6 nm)/Pt(10 nm)/Si and Ta(4 nm)/Cr(10 nm)/Pt(12 nm)/Si, noted PFP and TCP, respectively. As an example, Fig.1(a) and (b) show the simulated depth and angular distribution of the electric field in the PFP stack at the photon energies of the Fe Kα and Pt Lα emissions, respectively. It is clearly seen that waveguide modes are formed in the Fe layer (guiding layer) at glancing angles close to 0.6° and 0.4° for the Fe Kα and Pt Lα emissions, respectively. This means that when the angle of detection is equal to these angles, an intensity maximum is expected for the corresponding emission. Any shift of the positions of the Fe or Pt atoms from the designed layers should give different position and amplitude of their features in the PIXE-Kossel curve.

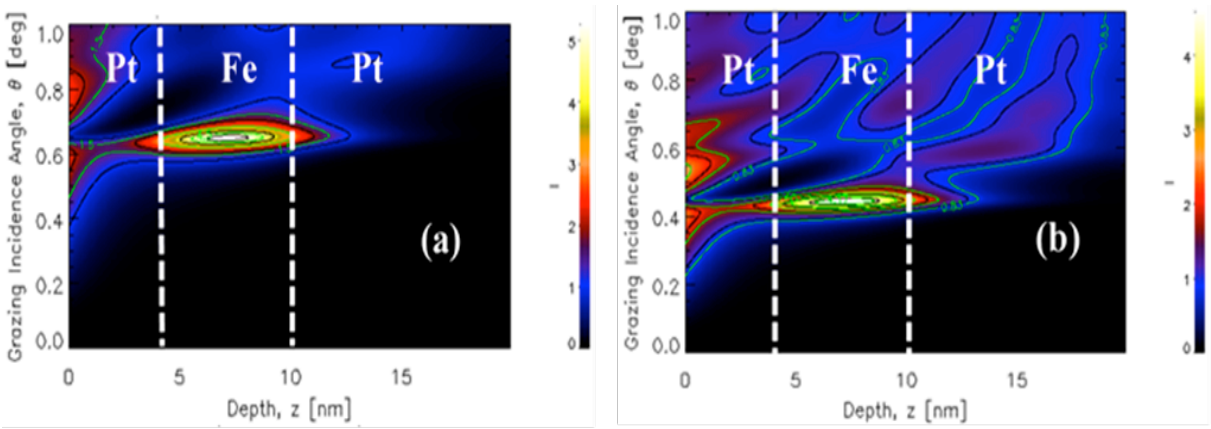


Fig. 1. Simulated depth and angular distribution of the electric field in the planar PFP X-ray waveguide at the photon energy corresponding to (a) the Fe Kα emission (6403 eV) and (b) the Pt Lα emission (9442 eV). The vertical color bar gives the intensity scale of the electric field.

The designed thin films were deposited at room temperature on a Si (100) substrate by magnetron sputtering. The power applied on the sputtering targets was 10 W, the base pressure was $10^{-8}$ mbar, and the sputtering gas was argon at the working pressure of $5\times10^{-2}$ mbar. The sputtering rates of Pt, Fe, Cr and Ta were 0.066, 0.024, 0.024 and 0.035 nm/s, respectively, as measured by a quartz microbalance.

### 2.2. Proton-induced X-ray emission

The schematic diagram of the PIXE-Kossel experiment is shown in Fig. 2. A 1.6 MeV proton beam generated by the Van de Graaff accelerator of the Système d'Analyse par Faisceaux d'Ions Rapides (SAFIR) platform, incident normal to the sample surface, was used to analyse the sample. An ANDOR iKon-M energy dispersive CCD camera equipped with a 1024×1024 sensor array and 13×13 μm pixels, was used to record the generated X-ray emissions. This CCD camera produces an X-ray spectrum for each of its pixels. Each column of pixels corresponds to a detection angle. To facilitate the data acquisition and subsequent data processing, a 4×4 binning is selected to obtain 256×256 pixel images (as shown in Fig. 2). The angular acceptance of the camera is 2.71°, as determined in Ref. [21]. The measurement time is 2 h with 24 collected frames. Each frame acquisition time was 5 min.

As shown in Fig. 2, when the proton beam irradiates the sample, we first obtain a picture on the CCD camera, where the intensity of a pixel depends on the total number of X-rays collected in this pixel. After the energy calibration of the spectrum, a region of interest (ROI) is selected around a characteristic line, to obtain a 256×256 filtered spectral image. Then, this image is integrated in the vertical direction so as to obtain a 256 channel scan, representing the intensity of the given line as a function of the detection angle (grazing exit angle θ), i.e. the Kossel curve.

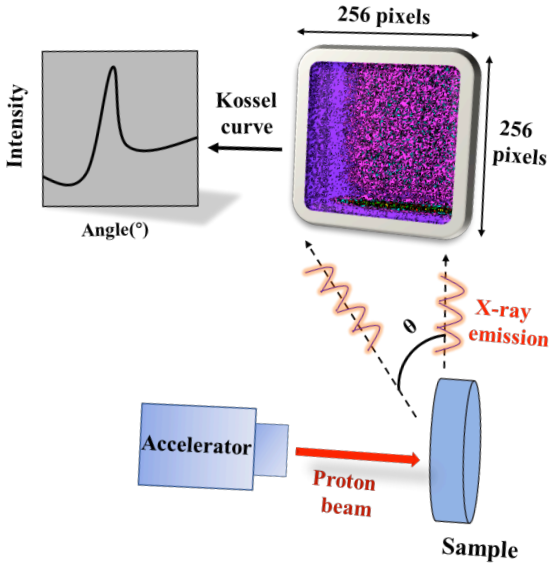


Fig. 2. Scheme of the experimental setup for the PIXE-Kossel experiment. The angular acceptance of the camera is 2.71°.

### 2.3. X-ray reflectivity

To know the actual thickness and roughness of the deposited stacks, X-ray reflectivity (XRR) measurement is conducted. XRR is widely employed to study thin films and multilayers. In this study, the XRR measurements were performed at the 0.154 nm wavelength on a Rigaku five-circle diffractometer. Each measurement time was about 40 min. Then with the help of the IMD software [28] and the optical constants of Ref. [29], the measured XRR curves were fitted to determine the thickness, roughness and density of the various layers.

## 3. Results and Discussions

### 3.1. Analysis of Pt (4 nm)/Fe (6 nm)/Pt (10 nm) film waveguide

The XRR curve of the PFP sample is shown in Fig. 3. It displays the scattered X-ray intensity (in logarithmic scale) as a function of the glancing angle. For the fitting procedure, no interfacial compound is firstly considered. The values of thickness and roughness of each layer obtained from the fitting results are listed in Table 1. The densities, determined with an uncertainty of 10%, are close to those of the bulks. The above structural parameters (density, thickness and roughness of the layers) are then applied to the calculation of Kossel curves. The simulation is performed with the FLUORT code [30]. Details of the Kossel curve simulation have been described in Ref. [21]. The simulation method is originally designed for X-ray fluorescence calculation under Kossel effect. It calculates the electric field generated within the stack by the emitted radiation according to the reciprocity theorem. In the calculation, all parameters (thicknesses of the layers and roughness of each interface) determined from XRR fitting are applied. The simulation results will then be compared with the experimental results.

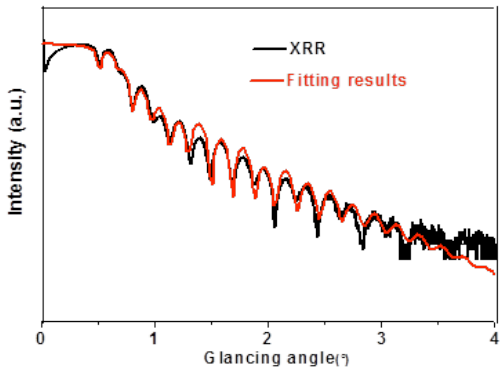


Fig. 3. Measured (black line) and fitted (red line) XRR curves of the PFP stack.

Table 1. Fitted values from XRR measurements of thickness, roughness and density of the different layers in the PFP stack (listed from the top layer to the substrate).

| | Thickness/Roughness (nm) (±0.05 nm) | Density |
|---|---|---|
| Pt | 4.62/0.60 | bulk |
| Fe | 6.65/0.80 | bulk |
| Pt | 11.06/0.77 | bulk |
| Si substrate | bulk/0.42 | bulk |

We then carry out the PIXE experiment and obtain the overall X-ray emission spectrum (intensity in logarithmic scale), as shown in Fig. 4. The spectrum is the sum of the spectra obtained over all the pixels of the CCD camera. The energy calibration of the spectrum is performed from the position of the Fe Kα, Fe Kβ, Pt Lα and Pt Lβ emissions. Only Fe Kα and Pt Lα Kossel curves are discussed here. To extract the Fe Kα and Pt Lα Kossel curves, we select ROI on the overall spectrum (shown in Fig. 5). The ROI range is chosen to minimize the influence of neighboring lines. The data processing is conducted using the PyMCA software [31].

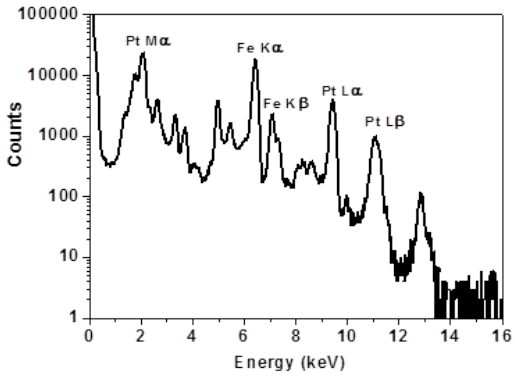


Fig. 4. X-ray emission spectrum of the PFP stack summed over all the pixels of the CCD camera.

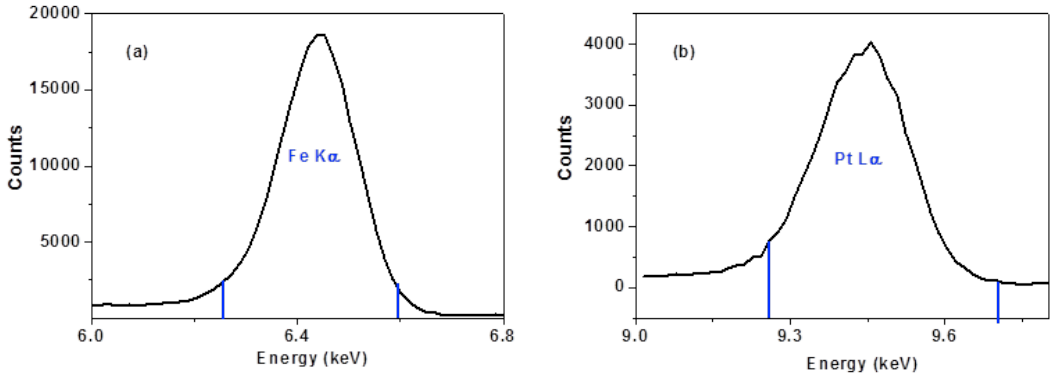


Fig. 5. Fe Kα (a) and Pt Lα (b) ROI selected on the X-ray emission spectrum of the PFP stack.

As an angular calibration is missing, we shift one experimental Kossel curve so that its main peak is at the same angle as the simulated one. The same shift is applied for all the Kossel curves. The simulated Kossel curves of the as-designed structure

Pt(4 nm)/Fe(6 nm)/Pt(10 nm), and of that having the structure given in Table 1 are compared in Fig. 6. For Fe Kα, the curves (Fig. 6(a)) present one main peak while the simulated curves of Pt Lα (Fig. 6(b)) show two main peaks. Due to the current fluctuation of PIXE apparatus (no current regulation), the generated Kossel curves are in part noisy. It is noticed that the main peaks of Fe Kα and Pt Lα Kossel curves appear at about 0.6° and 0.4° respectively, which are corresponding to the waveguide modes (in agreement with the results of Fig. 1). Small shifts of the main peaks are observed between the two simulations. We find that the main experimental features are almost reproduced by the simulated XRR curves. However, for the Fe Kα Kossel curve, the intensity toward higher angles has obvious difference, indicating that the description of the stack should be modified. The above results demonstrate that it is not enough to characterize the stack only according to the XRR fitting result.

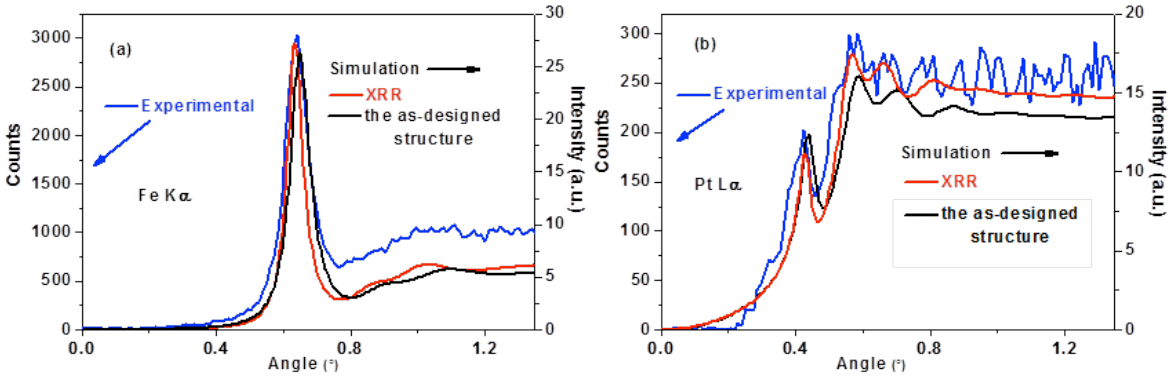


Fig. 6. Comparison of the experimental (blue line) and simulated Fe Kα (a) and Pt Lα (b) Kossel curves of the PFP stack. Simulated curves are obtained with the parameters both from the as-designed structure and from the structure fitting the XRR measurements (Table 1).

Composition variation of the stack is then considered to improve the fit. In Ref. [32], magneto-optical spectra of Pt/Fe multilayers were investigated. The comparison of the simulation and the experiment confirmed the formation of $Pt_{69}Fe_{31}$ alloy layer at the Pt-Fe interface. As a result, to improve the fitting result for the PFP stack, the presence of the interfacial compound $Pt_{69}Fe_{31}$ is taken into account at both Pt-on-Fe and Fe-on-Pt interfaces. The reflectivity curve and corresponding fit are presented in Fig. 7. After the consideration of $Pt_{69}Fe_{31}$ interlayers, the $\chi^2$ value

decreases, indicating the fitting result improves. The geometrical information of the stack obtained from the modified fit is listed in Table 2. It is also noticed that the thickness and roughness of $Pt_{69}Fe_{31}$ at the Pt-on-Fe interface are different to those at the Fe-on-Pt interface, indicating that the interfaces are asymmetrical. Based on the obtained structure information (Table 2), the Fe Kα and Pt Lα Kossel lines are simulated and then compared with the experimental ones. Fig. 8 shows the revised PIXE-Kossel simulations. The simulated XRR curves with introduction of $Pt_{69}Fe_{31}$ interlayers show a better agreement with the experimental ones than the previous simulations (Fig. 6). The difference between Fe Kα experimental and simulated Kossel curves at higher angles derives from the density and composition of $Pt_xFe_y$ intermixing layer. In this study, $Pt_{69}Fe_{31}$ interlayers are considered at both interfaces, which could efficiently reduce the discrepancy between experiment and simulation curve at higher angle. It is difficult to define the exact composition and density of the formed $Pt_xFe_y$ intermixing layer. But by the combination of XRR and PIXE-Kossel, it is convenient to know whether intermixing occurs.

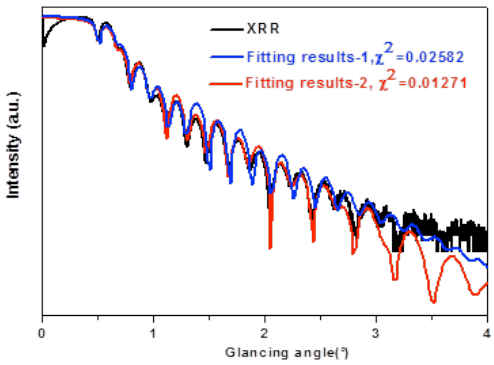


Fig. 7. Measured (black line) and fitted XRR curves of the PFP stack. Fitting result-1 (blue line) and Fitting result-2 (red line) represent the fitting results without and with the consideration of the presence of $Pt_{69}Fe_{31}$ interlayers at both interfaces.

Table 2. Fitted values from XRR measurements of thickness, roughness and density of the different layers in the PFP stack (listed from the top layer to the substrate) accounting for the presence of $Pt_{69}Fe_{31}$ interlayers at both interfaces.

| | Thickness/Roughness (nm) (±0.05 nm) | Density ($g/cm^3$) |
|---|---|---|
| Pt | 3.83/0.57 | bulk |
| $Pt_{69}Fe_{31}$ | 1.62/0.90 | 16 ± 2 |
| Fe | 5.19/1.20 | bulk |
| $Pt_{69}Fe_{31}$ | 1.41/0.79 | 16 ± 2 |
| Pt | 10.25/0.39 | bulk |
| Si substrate | bulk/0.50 | bulk |

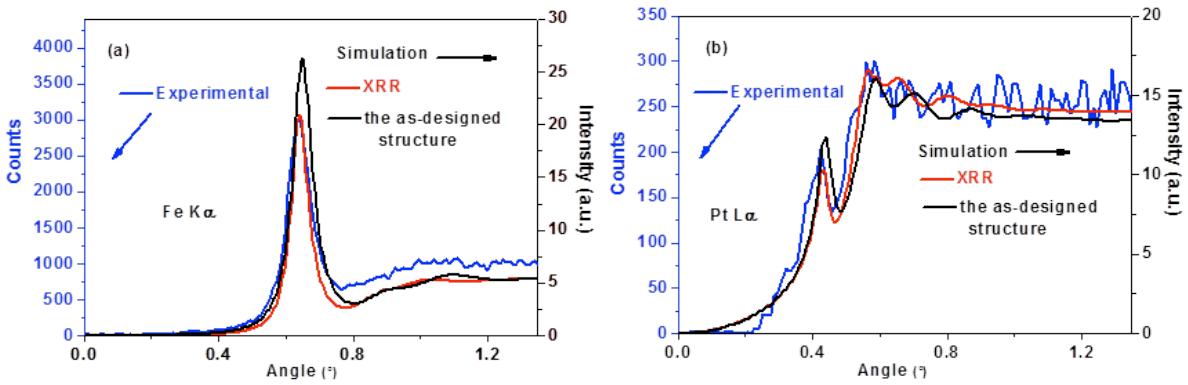


Fig. 8. Comparison of the experimental (blue line) and simulated Fe Kα (a) and Pt Lα (b) Kossel curves of the PFP stack. Simulated curves are obtained with the parameters both from the as-designed structure and from the structure fitting the XRR measurements (Table 2).

### 3.2. Analysis of Ta(4 nm)/Cr(10 nm)/Pt (12 nm) waveguide

Fig. 9 shows the measured and fitted XRR curves of the TCP stack. It is difficult to obtain a reliable fitting result if no oxidation of the designed structure (Ta/Cr/Pt) is considered. Owing to the protective ability of $Ta_2O_5$ compound against oxidization [33, 34], the $Ta_2O_5$/Cr/Pt structure is firstly considered. Again, fitting remains difficult if no oxidation of Cr is considered. It is reported that $Cr_2O_3$ (the oxidation product of Cr) also possesses good corrosion resistance, which is usually used for the protection of components operating in harsh chemical environments [35].

So the $Ta_2O_5$/$Cr_2O_3$/Cr/Pt structure is then taken into consideration. It is observed that although there exist some intensity discrepancies, the fit is well aligned with the measured XRR data. The obtained structural parameters of the stack are listed in

Table 3. The fitted thickness of $Ta_2O_5$ layer is almost two times higher than that of the original Ta layer. This could be explained by its lower density (bulk densities of Ta and $Ta_2O_5$ are 16.65 [29] and 8.2 g/cm$^3$ [36] respectively). Compared with Cr (bulk density of 7.19 g/cm$^3$), the bulk density $Cr_2O_3$ (5.21 g/cm$^3$ [29]) does not change too much. As a result, the sum of the fitted thicknesses of $Cr_2O_3$ and Cr layers is almost equal to the designed Cr layer thickness. From the fitted results, we note that the oxidation of the stack is major (total for Ta and partial for Cr), so that the studied stack differs substantially from the designed structure.

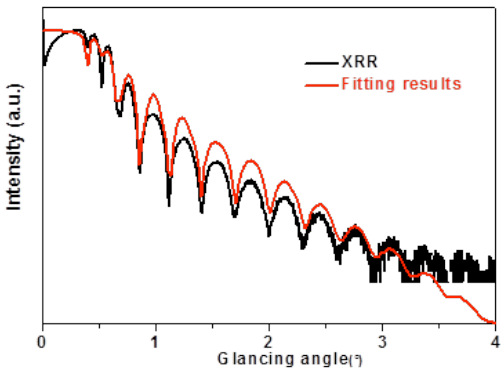


Fig. 9. Measured (black line) and fitted (red line) XRR curves of the TCP stack.

Table 3. Fitted values from XRR measurements of thickness, roughness and density of the different layers in the TCP stack (listed from the top layer to the substrate).

| | Thickness/Roughness (nm) (±0.05 nm) | Density |
|---|---|---|
| $Ta_2O_5$ | 7.87/1.09 | bulk |
| $Cr_2O_3$ | 6.55/1.30 | bulk |
| Cr | 4.54/0.80 | bulk |
| Pt | 13.79/0.54 | bulk |
| Si substrate | bulk/0.67 | bulk |

Fig. 10 shows the overall X-ray emission spectrum. The energy is calibrated from the positions of the Cr Kα, Ta Lα and Pt Lα emissions. Other peaks can be ascribed to the fluorescence of impurities inside the sample and/or of the experimental setup. Then Cr Kα, Ta Lα and Pt Lα Kossel curves are extracted similarly to those characteristic from the previous stack.

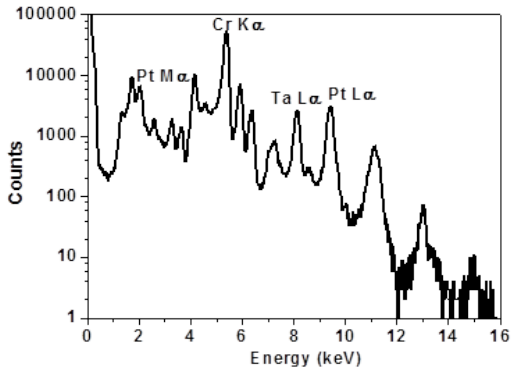


Fig. 10. X-ray emission spectrum of the TCP stack summed over all the pixels of the CCD camera.

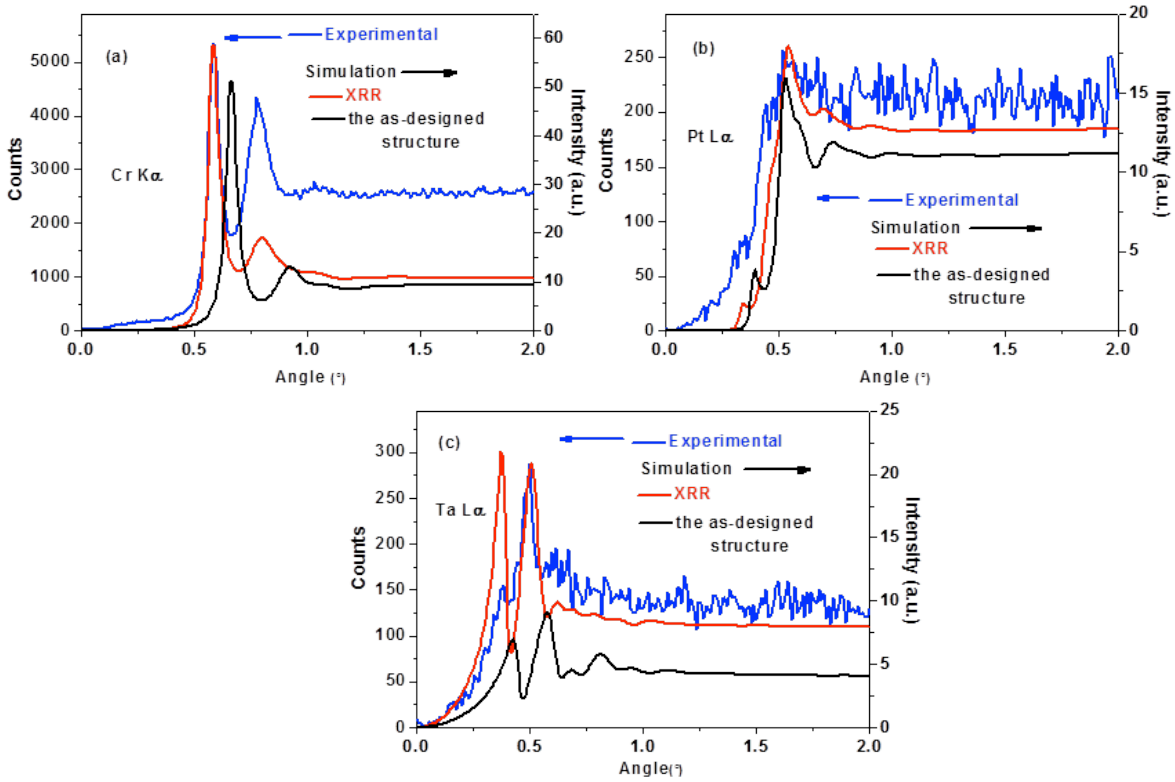


Fig. 11. Comparison of the experimental and simulated (see Table 3) Cr Kα (a), Pt Lα (b) and Ta Lα (c) Kossel curves.

Based on the structure obtained from XRR (Table 3), Kossel curve simulations are performed (shown in Fig. 11), which are also compared with the as-designed structure and the experiment for the Cr Kα, Pt Lα and Ta Lα emissions. It is clearly seen that the as-designed structure cannot reproduce the experiment since large

angular shifts and intensity discrepancies exist. Whereas the experimental Pt Lα curve (Fig. 11b) shows a reasonable agreement with the simulated one deduced from the XRR fit including oxidization effect, for the Cr Kα and Ta Lα curves (Fig. 11a and c) the relative intensities of the main features still exhibit obvious differences.

As a partial conclusion, since only introducing the oxidation of the stack does not allow fitting the experimental Kossel curves, we now study the possibility of compound formation. Due to the negative standard Gibbs energy of the reaction calculated with the HSC software [37] (Ta (s) + 2Cr (s) = $TaCr_2$ (s), $\Delta G$ = -26.83 kJ/mol at 25°C [38, 39]), we then assume that $TaCr_2$ is possibly formed between the Ta and Cr layers during the deposition process. Oxidation of the stack is then assumed when the sample is transferred in air. It has been reported that $CrTaO_4$ possesses good protective ability, which could decrease the oxidation rate of the underlying alloys [40, 41]. So the new stack description, $CrTaO_4/TaCr_2$/Cr/Pt, is applied in the XRR fitting process. The corresponding reflectivity curve and its fit are displayed in Fig. 12 while the structural parameters of the stack extracted from the fit are collected in Table 4. The obtained structure differs greatly from the as-designed structure and also from the previously considered oxidized stack (Table 3). Compared with the as-designed structure, the stack thickness change (Table 4) can be explained by the density variation of the layers. Based on the conservation of mass, when the designed Ta layer is consumed totally for the $TaCr_2$ formation, the thickness of the $TaCr_2$ layer will be 13.1 nm and the residual thickness of the Cr layer will be 4.7 nm. So the total thickness of $TaCr_2$ and Cr will be 17.8 nm (if no oxidation is considered). When oxidation occurs, as the fitted density difference of $CrTaO_4$ and $TaCr_2$ is small, the sum of the fitted thickness of $CrTaO_4$, $TaCr_2$ and Cr only changes a little, which is 18.73 nm.

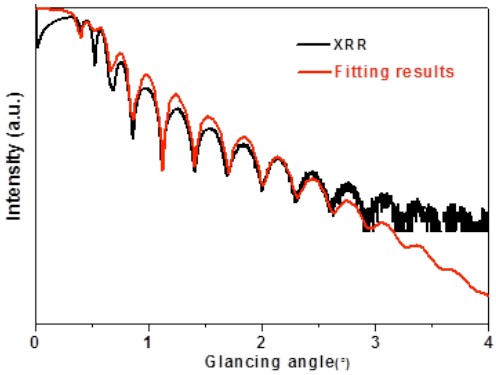


Fig. 12. Measured (black line) and fitted (red line) XRR curves of the TCP stack accounting for the compound formation and subsequent oxidation.

Table 4. Fitted values from XRR measurements of thickness, roughness and density of the different layers in the TCP stack (listed from the top layer to the substrate) accounting for the compound formation and subsequent oxidation.

| | Thickness/Roughness (nm) (±0.05 nm) | Density ($g/cm^3$) |
|---|---|---|
| $CrTaO_4$ | 10.75/1.10 | 6 ± 1 |
| $TaCr_2$ | 3.96/1.32 | 8 ± 1 |
| Cr | 4.02/0.53 | bulk |
| Pt | 13.79/0.54 | bulk |
| Si substrate | bulk/0.69 | bulk |

Fig. 13 shows the revised PIXE-Kossel simulations, which improve significantly. Compared with the simulation curves in Fig. 11, especially for the Cr Kα, the relative intensities are much closer to the experimental ones. Hence, according to the XRR (Fig. 12) and the Kossel (Fig. 13) results, it is anticipated that the new designed structure is close to the real structure of the TCP stack. However, a refinement of this structure is still in need to reach an even better fit of the Kossel curves. Particularly the large discrepancy for the Ta curve (Fig. 13b) probably originates from a wrong number and depth distribution of the Ta atoms. The non-uniform Ta depth distribution makes it more difficult to improve the result. The uncertainty could be reduced if the optical constants used in simulation were better known. In addition, precise definition of the angular calibration would be also helpful to decrease the difference.

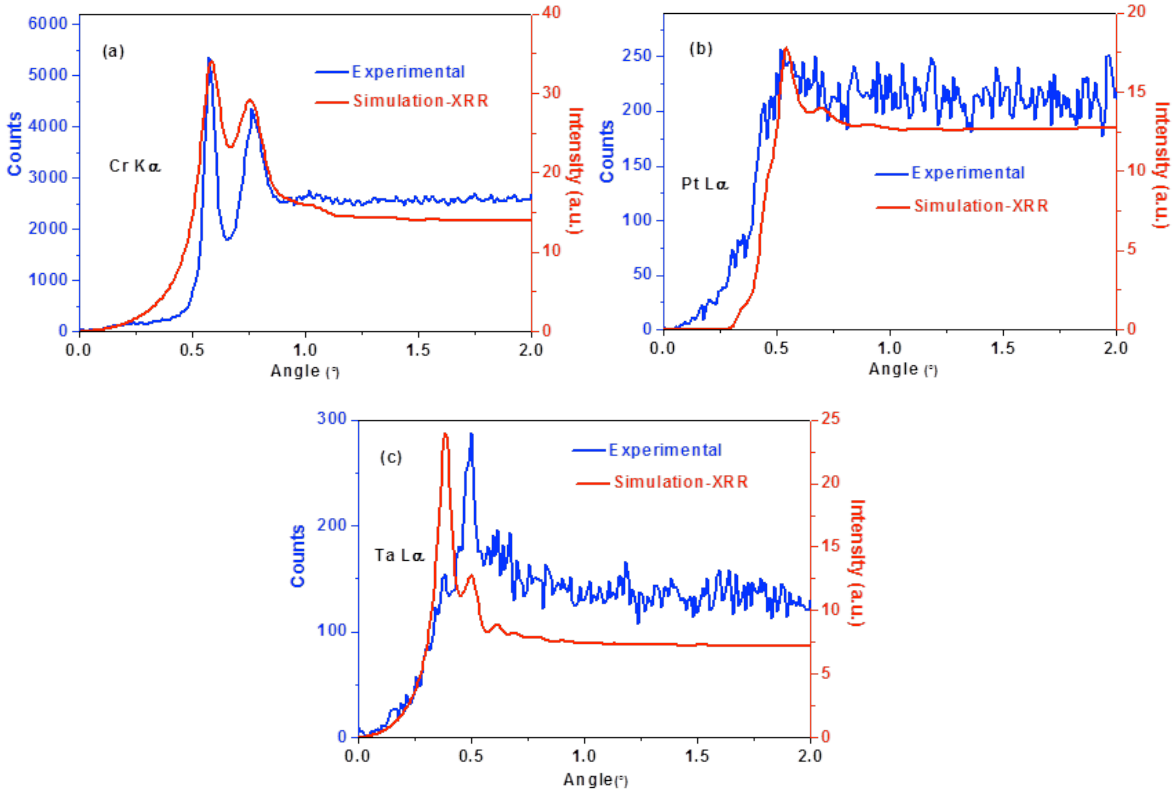


Fig. 13. Comparison of the experimental and revised simulated (see Table 4) Cr Kα (a), Pt Lα (b) and Ta Lα (c) Kossel curves.

## 4. Conclusions

We have studied the feasibility of observing and exploiting proton-induced X-ray emission in Kossel geometry in stacks consisting of only a few layers, many less than the number in periodic multilayers designed for X-ray optics. Pt/Fe/Pt and Ta/Cr/Pt nano-scale tri-layers were designed to be used as X-ray planar waveguides. In the waveguide configuration, owing to the high sensitivity of the electric field versus the detection direction of the emitted radiation, PIXE-Kossel curves are sensitive to the depth distribution of the emitting atoms. In addition, the prepared stacks were also investigated by grazing incident X-ray reflectometry.

For all systems, the as-designed parameters (thickness, roughness and density of the layers) fail to generate both XRR and PIXE-Kossel simulated curves reproducing the experimental ones. It is always possible to find a structure able to reproduce the XRR curve, by considering some oxidation or the formation of some interfacial compound for example, but then the PIXE-Kossel curve simulations still differ

markedly from the experimental ones. To get a satisfying agreement between experiment and simulation for both XRR and PIXE-Kossel curves, we had to consider that interlayers form at the interfaces of the Pt/Fe/Pt waveguide, while in the Ta/Cr/Pt system, some intermixing takes place between the Ta and Cr layers to form a compound, which is subsequently partly oxidized. This work demonstrates the ability of the PIXE-Kossel methodology to characterize the stacks of nano-scale thin films.

**Acknowledgement**

This work has been supported by the mobility scholarship within the framework of the Erasmus+ International Credit Mobility Program and the China Scholarship Council (CSC) scholarship within a CSC-Sorbonne University (SU) doctoral program. N. Casaretto and Y. Zheng from INSP are thanked for performing the XRR experiments.

**References**

[1] W. Kossel, V. Loeck, H. Voges, Die Richtungsverteilung der in einem Kristall entstandenen charakteristischen Röntgenstrahlung, Zeitschrift für Physik 94 (1935) 139-144, https://doi.org/10.1007/BF01330803

[2] R. Tixier, C. Wache, Kossel patterns, J. Appl. Crystallogr. 3 (1970) 466-485, https://doi.org/10.1107/S0021889870006726

[3] J.A. Martínez-González, X. Li, M. Sadati, Y. Zhou, R. Zhang, P.F. Nealey, J.J. de Pablo, Directed self-assembly of liquid crystalline blue-phases into ideal single-crystals, Nat. Commun. 8 (2017) 15854, https://doi.org/10.1038/ncomms15854

[4] E. Langer, S. Däbritz, C. Schurig, W. Hauffe, Lattice constant determination from Kossel patterns observed by CCD camera, Appl. Surf. Sci. 179 (2001) 45-48, https://doi.org/10.1016/S0169-4332(01)00261-6

[5] P. Jonnard, J.-M. André, C. Bonnelle, F. Bridou, B. Pardo, Soft-x-ray Kossel structures from W/C multilayers under various electron ionization conditions, Phys. Rev. A. 68 (2003) 032505, https://doi.org/10.1103/PhysRevA.68.032505

[6] A.C. Aiken, P.F. DeCarlo, J.L. Jimenez, Elemental analysis of organic species with electron ionization high-resolution mass spectrometry, Anal. Chem. 79 (2007) 8350-8358, https://doi.org/10.1021/ac071150w

[7] J.I. Goldstein, D.E. Newbury, J.R. Michael, N.W. Ritchie, J.H.J. Scott, D.C. Joy, Scanning electron microscopy and X-ray microanalysis, Springer, 2017, https://doi.org/10.1007/978-1-4613-0491-3

[8] A. Rousse, K.T. Phuoc, R. Shah, A. Pukhov, E. Lefebvre, V. Malka, S. Kiselev, F. Burgy, J.-P. Rousseau, D. Umstadter, Production of a keV X-ray beam from synchrotron radiation in relativistic laser-plasma interaction, Phys. Rev. Lett. 93 (2004) 135005, https://doi.org/10.1103/PhysRevLett.93.135005

[9] P. Jonnard, Y. Yuan, K. Le Guen, J.-M. André, J. Zhu, Z. Wang, F. Bridou, Spontaneous soft x-ray fluorescence from a superlattice under Kossel diffraction conditions, J. Phys. B At. Mol. Opt. Phys. 47 (2014) 165601, https://doi.org/10.1088/0953-4075/47/16/165601
[10] F. Lucarelli, G. Calzolai, M. Chiari, M. Giannoni, D. Mochi, S. Nava, L. Carraresi, The upgraded external-beam PIXE/PIGE set-up at LABEC for very fast measurements on aerosol samples, Nucl. Instrum. Methods Phys. Res. Sect. B Beam Interact. Mater. At. 318 (2014) 55-59, https://doi.org/10.1016/j.nimb.2013.05.099
[11] A. Subercaze, C. Koumeir, V. Métivier, N. Servagent, A. Guertin, F. Haddad, High energy PIXE: A tool to characterize multi-layer thick samples, Nucl. Instrum. Methods Phys. Res. Sect. B Beam Interact. Mater. At. 417 (2018) 41-45, https://doi.org/10.1016/j.nimb.2017.09.009
[12] K. Le. Guen, J.M. André, M. Wu, V. Ilakovac, F. Delmotte, S. Rossi, F. Bridou, E. Meltchakov, A. Giglia, S. Nannarone, Z. Wang, Q. Huang, Z. Zhang, J. Zhu, Y. Tu, Y. Yuan, I. Vickridge, D. Schmaus, E. Briand, S. Steydli, P. Walter, P. Jonnard, Kossel Effect in Periodic Multilayers, J. Nanosci. Nanotechno. 19 (2019) 593-601, https://doi.org/10.1166/jnn.2019.16472
[13] J. Baumann, C. Herzog, M. Spanier, D. Grötzsch, L. Lühl, K. Witte, A. Jonas, S. Günther, F. Förste, R. Hartmann, M. Huth, D. Kalok, D. Steigenhöfer, M. Krämer, T. Holz, R. Dietsch, L. Strüder, B. Kanngießer, I. Mantouvalou, Laboratory Setup for Scanning-Free Grazing Emission X-ray Fluorescence, Anal. Chem., 89 (2017) 1965-1971, https://doi.org/10.1021/acs.analchem.6b04449
[14] V. Szwedowski-Rammert, J. Baumann, C. Schlesiger, U. Waldschläger, A. Gross, B. Kanngießer, I. Mantouvalou, Laboratory based GIXRF and GEXRF spectrometers for multilayer structure investigations, J. Anal. At. Spectrom. (2019), https://doi.org/10.1039/C8JA00427G
[15] D.L. Gil, D. Windover, Limitations of X-ray reflectometry in the presence of surface contamination, J. Phys. D: Appl. Phys. 45(2012) 235301, https://doi.org/10.1088/0022-3727/45/23/235301
[16] J. Spear, H. Murakami, S. Terada, Advances in X-ray Reflectivity (XRR) and X-ray Fluorescence (XRF) Measurements Provide Unique Advantages for Semiconductor Applications, in, 2003. AIP Conference Proceedings 683(2003) 646-650683; https://doi.org/10.1063/1.1622539
[17] D. Ingerle, M. Schiebl, C. Streli, P. Wobrauschek, Combination of grazing incidence x-ray fluorescence with x-ray reflectivity in one table-top spectrometer for improved characterization of thin layer and implants on/in silicon wafers, Rev. Sci. Instrum. 85 (2014) 083110, https://doi.org/10.1063/1.4893383
[18] X. Yang, W. Li, J. Zhu, X. Li, Z. Wang, Structural characterization of multilayer using the analysis combining GIXRF with GIXRR method, Eighth International Conference on Thin Film Physics and Applications 90680X (2013) https://doi.org/10.1117/12.2053960
[19] P. Hönicke, Y. Kayser, B. Beckhoff, M. Müller, J.-C. Dousse, J. Hoszowska, S.H. Nowak, Characterization of ultra-shallow aluminum implants in silicon by grazing incidence and grazing emission X-ray fluorescence spectroscopy, J. Anal. At.

Spectrom.27 (2012) 1432-1438, https://doi.org/10.1039/C2JA10385K
[20] M. Wu, K. Le Guen, J.-M. André, V. Ilakovac, I. Vickridge, D. Schmaus, E. Briand, S. Steydli, C. Burcklen, F. Bridou, E. Meltchakov, S. de Rossi, F. Delmotte, P. Jonnard, Kossel interferences of proton-induced X-ray emission lines in periodic multilayers, Nucl.Instrum. Methods Phys. Res. Sect. B Beam Interact. Mater. At. 386 (2016) 39-43, https://doi.org/10.1016/j.nimb.2016.09.014
[21] M. Wu, K. Le Guen, J.-M. André, P. Jonnard, I. Vickridge, D. Schmaus, E. Briand, P. Walter, Q. Huang, Z. Wang, Kossel diffraction observed with X-ray color camera during PIXE of nano-scale periodic multilayer, Nucl. Instrum. Methods Phys. Res. Sect. B Beam Interact. Mater. At. (2019), https://doi.org/10.1016/j.nimb.2018.08.008
[22] P. Midy, I. Brissaud, Application of a new algorithm to depth profiling by PIXE, Nucl. Instrum. Methods Phys. Res. Sect. B Beam Interact. Mater. At. 103 (1995) 489-493, https://doi.org/10.1016/0168-583X(95)00659-1
[23] S.A. Johansson, J.L. Campbell, K.G. Malmqvist, J.D. Winefordner, Particle-induced X-ray emission spectrometry (PIXE), John Wiley & Sons, 1995.
[24] A. Jarre, C. Fuhse, C. Ollinger, J. Seeger, R. Tucoulou, T. Salditt, Two-dimensional hard x-ray beam compression by combined focusing and waveguide optics, Phys. Rev. Lett. 94 (2005) 074801, https://doi.org/10.1103/PhysRevLett.94.074801
[25] T. Salditt, M. Osterhoff, M. Krenkel, R.N. Wilke, M. Priebe, M. Bartels, S. Kalbfleisch, M. Sprung, Compound focusing mirror and X-ray waveguide optics for coherent imaging and nano-diffraction, J. Synchrotron Radiat. 22 (2015) 867-878, https://doi.org/10.1107/S1600577515007742
[26] S. Hoffmann-Urlaub, P. Höhne, M. Kanbach, T. Salditt, Advances in fabrication of X-ray waveguides, Microelectron. Eng. 164 (2016) 135-138, https://doi.org/10.1016/j.mee.2016.07.010
[27] K. Hayashi, K. Sakai, H. Takenaka, Monochromatization of characteristic X-rays using stepped X-ray waveguide, Thin Solid Films 515 (2007) 5728-5731, https://doi.org/10.1016/j.tsf.2006.12.017
[28] D.L. Windt, IMD—Software for modeling the optical properties of multilayer films, Computers in physics 12 (1998) 360-370, https://doi.org/10.1063/1.168689
[29] B. Henke, CXRO database for x-ray attenuation length, in, http://henke.lbl.gov/optical_constants/
[30] J.-P. Chauvineau, F. Bridou, Analyse angulaire de la fluorescence du fer dans une multicouche périodique Fe/C, Le Journal de Physique IV 6 (1996) C7-53-C57-64, http://dx.doi.org/10.1051/jp4:1996707
[31] V. Solé, E. Papillon, M. Cotte, P. Walter, J. Susini, A multiplatform code for the analysis of energy-dispersive X-ray fluorescence spectra, Spectrochimica Acta Part B: Atomic Spectroscopy 62 (2007) 63-68, https://doi.org/10.1016/j.sab.2006.12.002
[32] K. Sato, H. Hongu, H. Ikekame, J. Watanabe, K. Tsuzukiyama, Y. Togami, M. Fujisawa, T. Fukazawa, Magnetooptical Spectra in Pt/Co and Pt/Fe Multilayers, Japanese Journal of Applied Physics 31 (1992) 3603, http://dx.doi.org/10.1143/JJAP.31.3603

[33] B. Díaz, J. Światowska, V. Maurice, M. Pisarek, A. Seyeux, S. Zanna, S. Tervakangas, J. Kolehmainen, P. Marcus, Chromium and tantalum oxide nanocoatings prepared by filtered cathodic arc deposition for corrosion protection of carbon steel, Surf.Coat.Technol.206(2012)3903-3910,https://doi.org/10.1016/j.surfcoat.2012.03.048
[34] W. Hu, J. Xu, X. Lu, D. Hu, H. Tao, P. Munroe, Z.-H. Xie, Corrosion and wear behaviours of a reactive-sputter-deposited Ta2O5 nanoceramic coating, Appl. Surf. Sci. 368 (2016) 177-190, https://doi.org/10.1016/j.apsusc.2016.02.014
[35] H. Asteman, M. Spiegel, A comparison of the oxidation behaviours of $Al_2O_3$ formers and $Cr_2O_3$ formers at 700 °C–Oxide solid solutions acting as a template for nucleation,Corros.Sci.50(2008)1734-1743,https://doi.org/10.1016/j.corsci.2007.12.012
[36] M. Hüppauff, K. Bange, B. Lengeler, Density, thickness and interface roughness of $SiO_2$, $TiO_2$ and $Ta_2O_5$ films on BK-7 glasses analyzed by x-ray reflection, Thin Solid Films 230 (1993) 191-198, https://doi.org/10.1016/0040-6090(93)90514-P
[37] A. Roine, HSC Chemistry® for Windows, Chemical Reaction and Equilibrium Software with Extensive Thermochemical Database, Version 5.0, Pori, (Finland). Outokumpu Research Oy, Information Service, PO Box 60 (2002)
[38] M.W. Chase Jr, NIST-JANAF thermochemical tables, J. Phys. Chem. Ref. Data, Monograph 9 (1998), https://doi.org/10.18434/T42S31
[39] S.G.T. Europe, Thermodynamic properties of inorganic materials, Landolt-Boernstein New Series, Group IV (1999), https://doi.org/10.1007/b72359
[40] M. Li, X. Sun, J. Li, Z. Zhang, T. Jin, H. Guan, Z. Hu, Oxidation behavior of a single-crystal Ni-base superalloy in air. I: at 800 and 900 °C, Oxid. Met. 59 (2003) 591-605, https://doi.org/10.1023/A:1023604214245
[41] W. Ren, F. Ouyang, B. Ding, Y. Zhong, J. Yu, Z. Ren, L. Zhou, The influence of $CrTaO_4$ layer on the oxidation behavior of a directionally-solidified nickel-based superalloy at 850–900° C, J. Alloys Compd. 724 (2017) 565-574, https://doi.org/10.1016/j.jallcom.2017.07.066